Supplementary Information

Facile synthesis of self-stabilized lamellar mica membrane for efficient organic solvent nanofiltration

Mingbo Xie[a,b,c,#], Huacun Li[a,b,c], Jinkang Liu[a,b,c], Jun Xie[a,b,c], Xu Yan[a,b,c], Qingwei Wang[a,b,c], Meiqing Shi[a,b,c], Liyuan Chai[a,b,c], Liyuan Zhang[a,b,c,*]

a School of Metallurgy and Environment, Central South University, Changsha, 410083, China

b Chinese National Engineering Research Center for Control & Treatment of Heavy Metal Pollution, Changsha 410083, China

c State Key Laboratory of Advanced Metallurgy for Non-ferrous Metals, Changsha 410083, China

* Corresponding authors: atomic_liyuan@yeah.net or atomic_liyuan@csu.edu.cn (L. Zhang)

1. Experimental Section

1.1 Chemical reagents

Mica ore is mined from Shangrao City, Jiangxin Province, China. The following materials were provided by the respective companies: Lithium chloride, Eriochrome Black T (EBT), and Methyl Orange (MO) by Shanghai McLin Biotech Co., Ltd.; Evans Blue (EB), Methyl Blue (MB), and Congo Red (CR) by Shanghai Aladdin Biochemical Technology Co., Ltd.; Vermiculite powder by Xinjiang Yuli Xinlong Vermiculite Co., Ltd.; Montmorillonite powder by Guzhang County Shanlin Stone Language Mineral Products Co., Ltd.; anhydrous ethanol by Tianjin Hengxing Chemical Reagent Manufacturing Co., Ltd.; 1-Butanol, Isopropanol, Methanol, and Acetonitrile by Shanghai Aladdin Biochemical Technology Co., Ltd. The nylon membrane and polyvinylidene fluoride (PVDF) membrane with a pore size of approximately 0.22 μm was purchased from Longjin Membrane Technology Co., Ltd. Deionized water was used throughout the entire experimental process.

1.2 Preparation of Mica, vermiculite, and montmorillonite nanosheet dispersions.

Clay particles (mica particles (MiP), vermiculite particles (VP), montmorillonite particles (MoP)) were first crushed into powders using an electric ore crusher and then sieved through a 200-mesh screen to obtain fine powders with a particle size of <75 μm. The improved lithium nitrate fusion method was applied: the clay powders were mixed with lithium nitrate at a mass ratio of 1:17, and the mixture was heated in an air atmosphere at a rate of 5°C/min to 350°C, followed by continuous heating for 12 hours and cooling to room temperature. A small amount of water was added, and the mixture was stirred until the lithium nitrate was fully dissolved[1]. Lithium ions intercalation was completed by stirring at 95°C for 12 hours. The solution was then centrifuged at 8000 rpm, and the supernatant was discarded. The excess lithium nitrate was removed by repeated washing with deionized water through centrifugation for 3-5 cycles. The mixture was then processed using an electric homogenizer at 10,000 rpm for 30 minutes, followed by ultrasonic treatment at 400W for 30 minutes to enhance exfoliation. Finally, the dispersion was centrifuged at 2000 rpm to remove

the precipitate, yielding a clay mineral nanosheet suspension.

1.3 Preparation of Clay membranes by the vacuum filtration method.

A certain amount of clay mineral nanosheet dispersion was diluted in pure water to a volume of 30 mL. The dispersion was then filtered onto a smooth polyvinylidene fluoride (PVDF) membrane using a vacuum filtration apparatus to form an ultrathin loading layer[2]. The membrane was dried in an oven at 60°C for 12 hours to obtain the clay membranes (mica membrane (MiM), vermiculite membrane (VM), montmorillonite membrane (MoM)). For the preparation of self-supporting membranes, a rough PVDF base membrane was used, and the clay loading was increased, allowing the membrane to be peeled off from the base membrane after drying.

1.4 Membrane organic solvent nanofiltration (OSN) Performance

The OSN performance of the clay membranes was tested using a duplex low-pressure cross-flow flat membrane test device. The testing pressure was 1 bar, with a flow rate of 2 L/min and a feed dye solution concentration of 20 mg/L. The effective testing area of the membrane was a rectangular region of 2 × 4 cm. Prior to the formal dye rejection tests, the membrane was pre-run with pure solvent at 1 bar for 30 minutes until the flow rate stabilized, after which the dye solution was tested. All tests were conducted at room temperature. Various dyes with different molecular weights, including EB, MB, CR, EBT, and MO, were selected for the OSN performance evaluation. Pure solvent permeation tests were performed under the same conditions, with the dye solution replaced by the solvent to be tested. Membrane permeation flux P ($L \cdot m^{-2} h^{-1} bar^{-1}$, abbreviated as LMH/bar) was calculated by first collecting the permeate at the permeate side, weighing the liquid with an electronic balance (0.0001 g), and then converting the weight to the corresponding volume using the solvent density. The flux was calculated using equation (1), with three repeated tests conducted for each sample to ensure reproducibility.

$$P = \frac{V}{A \times t \times p} \quad (1)$$

Where A (m^2) is the effective membrane area, t (h) is the permeation time , and p (bar) is the operating pressure.

The molecular sieving ability of the clay membranes was measured using a UV-Vis spectrophotometer to determine the absorbance at relevant peaks. A concentration standard curve was established by correlating absorbance with concentration, which was used to evaluate the concentrations of the feed and permeate solutions. Three repeated tests were conducted for each sample to ensure reproducibility. The rejection rate (R) was calculated using equation (2):

$$R = \left(1 - \frac{C_p}{C_f}\right) \times 100\% \quad (2)$$

Where C_f (mg/L) is the dye concentration in the feed solution , and C_p (mg/L) is the dye concentration in the permeate solution.

1.5 Characterization

The clay minerals powder and the prepared membranes were characterized using X-ray powder diffraction (XRD, MiniFlex600, Rigaku, Japan). The interlayer spacing was characterized by performing a wet membrane test, which involved soaking the membrane in a solution and quickly removing it to avoid solvent evaporation-induced shrinkage of the interlayer spacing. X-ray photoelectron spectroscopy (XPS, PHI Versa Probe 4, ULVAC-PHI, Japan) and attenuated total reflection Fourier transform infrared spectroscopy (ATR-FTIR, Nicolet iS50, Thermo Fisher Scientific, UK) were used to analyze the chemical structural changes of the clay particles and membranes. The particle morphology and surface and cross-sectional morphology of the membrane were examined using a field emission scanning electron microscope (FESEM, JSM-7610 FPlus, JEOL, Japan). The mechanical properties of the membranes were tested on an electronic universal testing machine (CMT6103, Meters Industrial Systems, China) by cutting the membranes into strips of 1 * 7cm. Each kind of membranes was tested at least three times. The size and thickness distribution of the clay mineral nanosheets were measured using an atomic force microscope (AFM, Dimension Icon, USA). Dye concentrations in the feed and permeate solutions were

measured using a UV-Vis spectrometer (U-4100, Hitachi Systems, Hokkaido, China).

2. Data

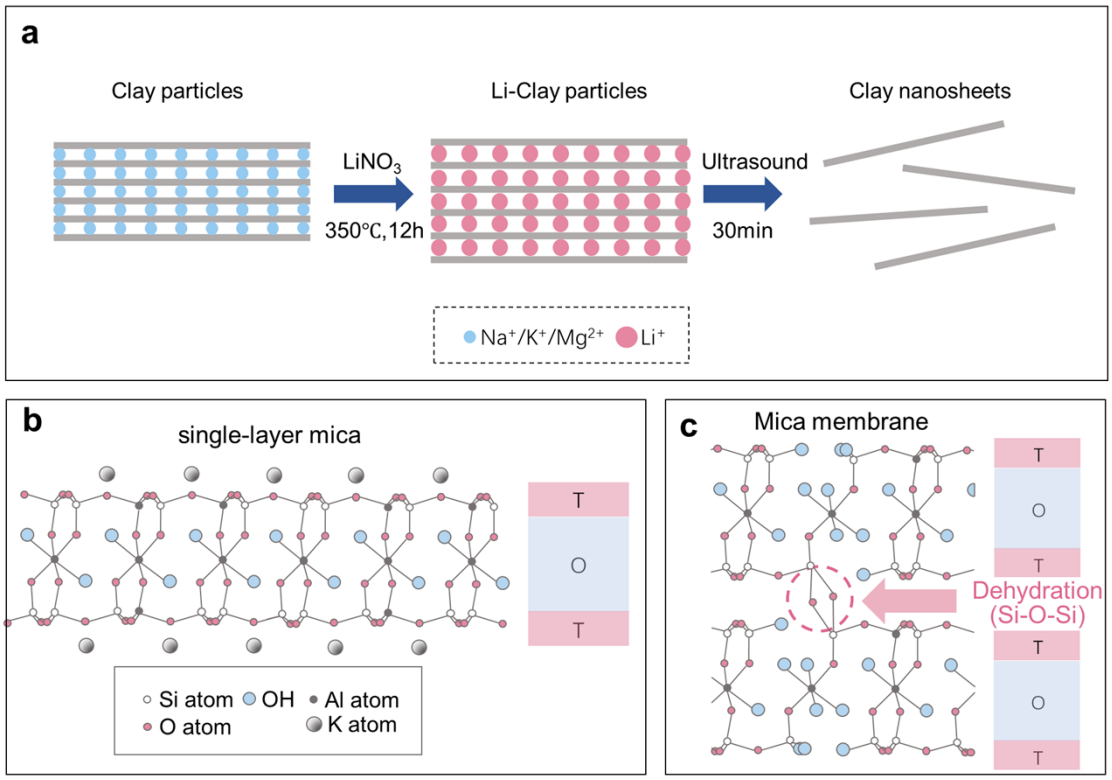

Figure S1. (a) Schematic diagram of the lithium nitrate intercalation and exfoliation process of clay mineral particles. MiP, VP, and MoP were used to enhance lithium ions intercalation in molten lithium nitrate, exchange interlayer ions, and expand the interlayer spacing, followed by ultrasonic-assisted exfoliation to obtain a suspension of clay mineral nanosheets. **(b) Schematic diagram of chemical structure of mica minerals; (c) Schematic diagram of chemical structure of mica membrane.** A single mica sheet is composed of a T-O-T structure , where the T layer is a silicon-oxygen tetrahedral structure (note: within the T layer one-quarter of the silicon atoms are replaced by aluminum) and the O layer is an aluminum-oxygen octahedral structure. In our work, the key Si-O-Si bridge structure referred to the formation of interlayer Si-O-Si between the single mica sheets (As indicated by the arrow), but not the Si-O-Si within the T structure .

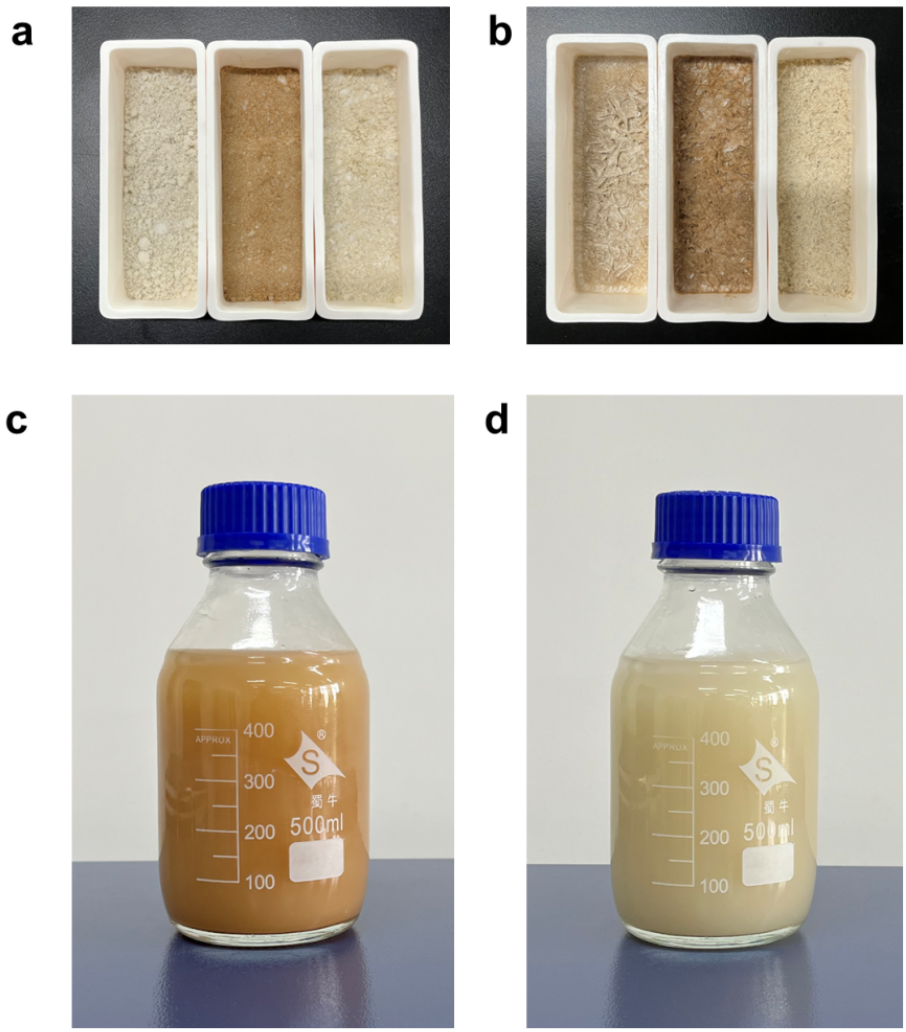

Figure S2. Photos of clay sample during interlayer stripping process. (a) Photographs of MiP, VP, MoP, and lithium nitrate mixture; (b) Photographs of mica, vermiculite, montmorillonite, and lithium nitrate molten salt intercalation, showing the formation of a solid block after cooling, indicating complete mixing in the molten salt state; (c) Dispersion of vermiculite nanosheets; (d) Dispersion of montmorillonite nanosheets.

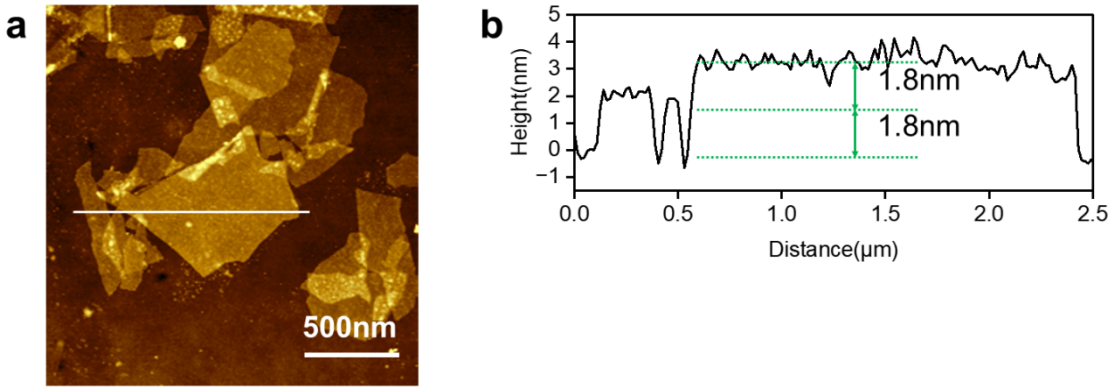

Figure S3. (a) Atomic force microscopy (AFM) image of mica nanosheets on a silicon substrate; (b) the sectional height distribution along the white line of fig. (a).

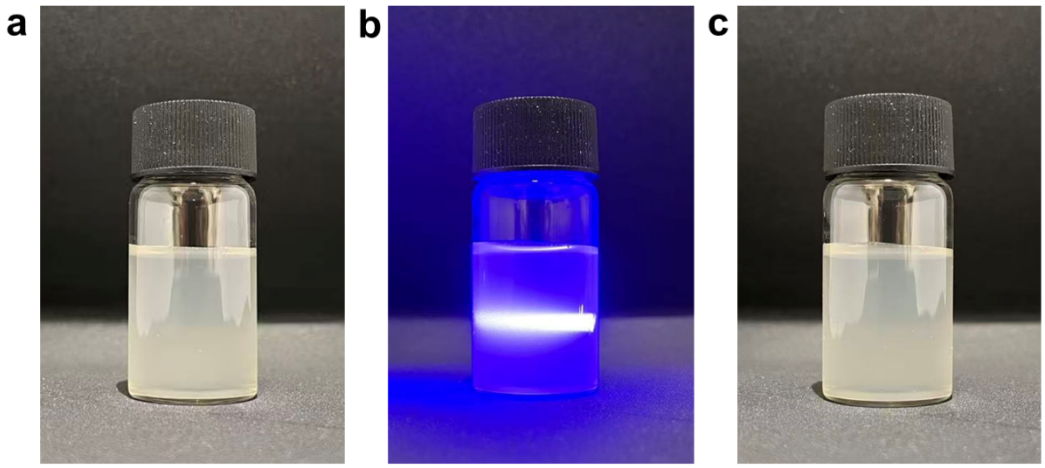

Figure S4. (a) photograph of the mica suspension; (b) Tyndall effect photograph of the mica suspension; (c) photograph of the mica suspension after 30 days.

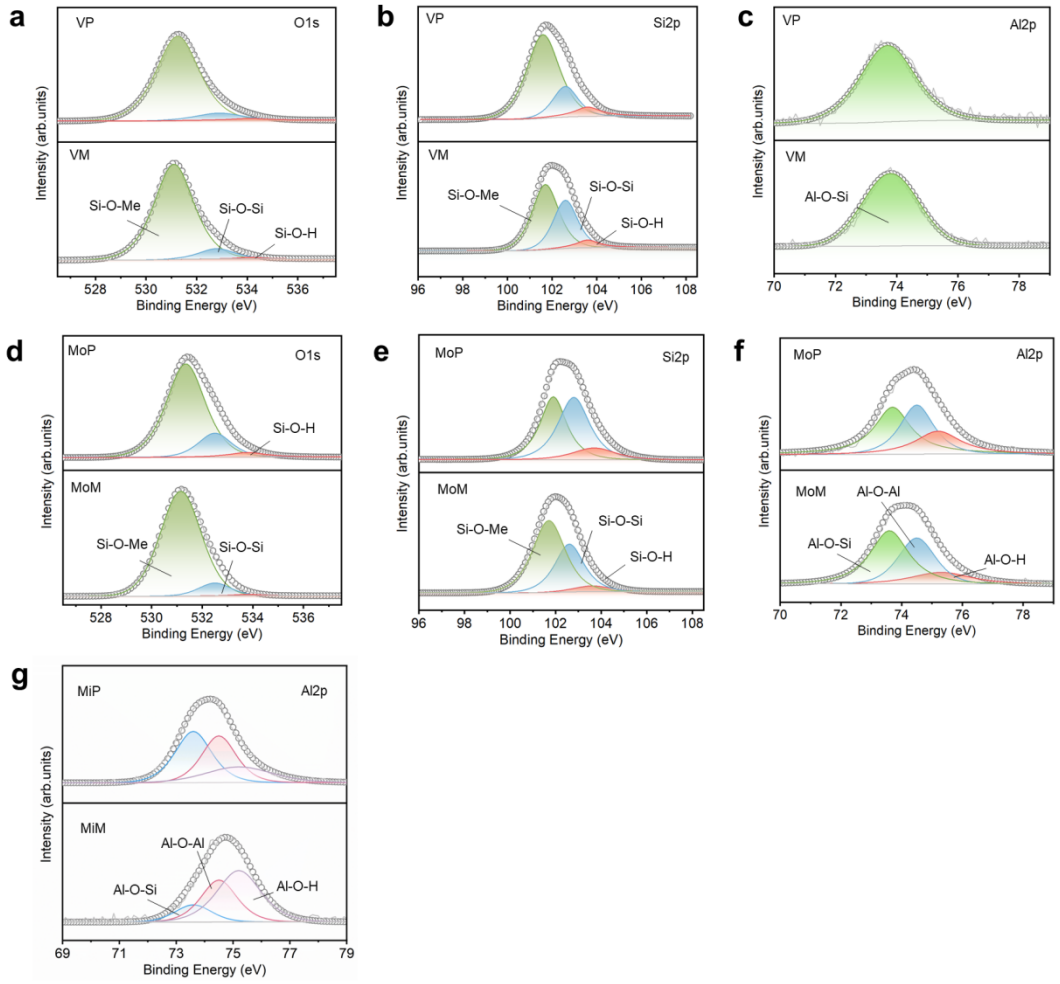

Figure S5. (a-c) XPS spectra of O 1s, Si 2p, and Al 2p for VP to VM; (d-f) XPS spectra of O 1s, Si 2p, and Al 2p for MoP to MoM; (g) XPS spectra of Al 2p for MiP to MiM.

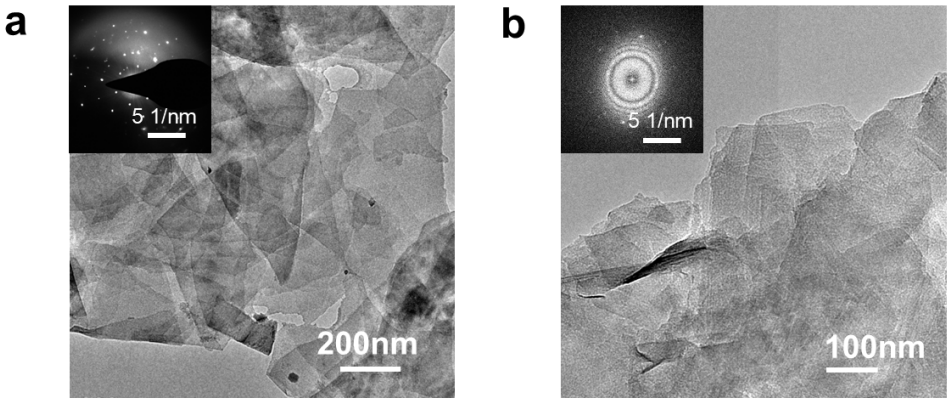

Figure S6. (a-b) Transmission electron microscopy (TEM) images of vermiculite and montmorillonite nanosheets, with insets showing electron diffraction patterns of vermiculite and montmorillonite crystals.

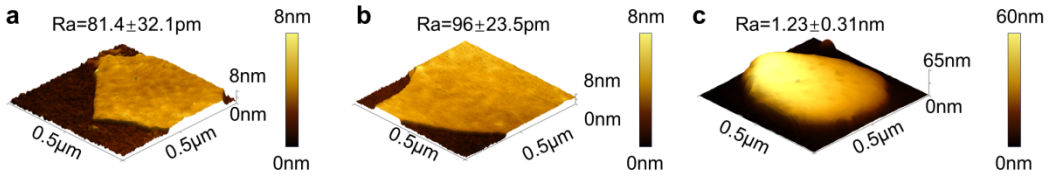

Figure S7. (a-c) Atomic force microscopy (AFM) 3D images and surface roughness of individual mica, vermiculite, and montmorillonite nanosheets.

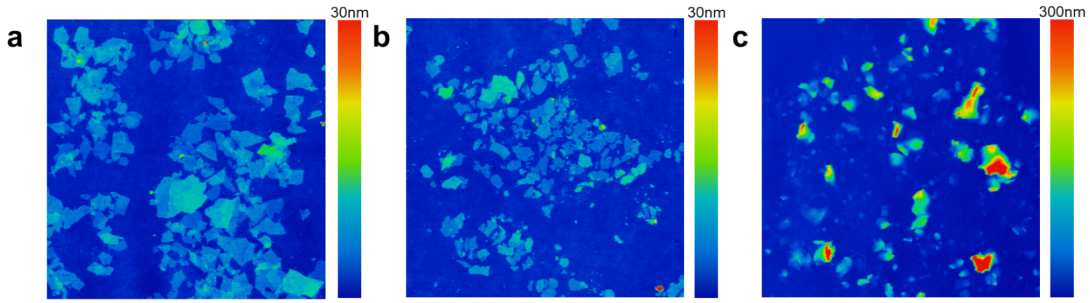

Figure S8. (a-c)AFM images of mica, vermiculite, and montmorillonite nanosheets.

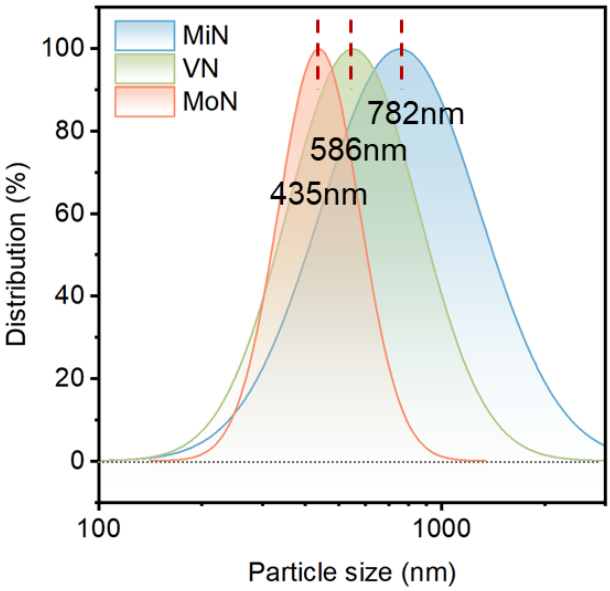

Figure S9. Particle size distribution of mica, vermiculite, and montmorillonite nanosheets.

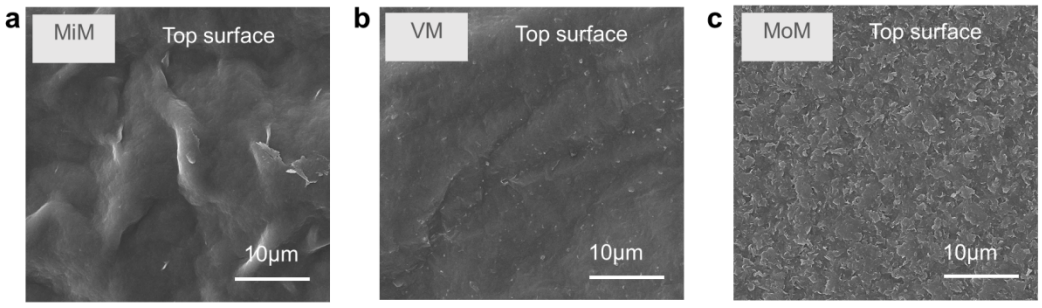

Figure S10. (a-c) Scanning electron microscopy (SEM) images of the top surface of MiM, VM, and MoM membranes.

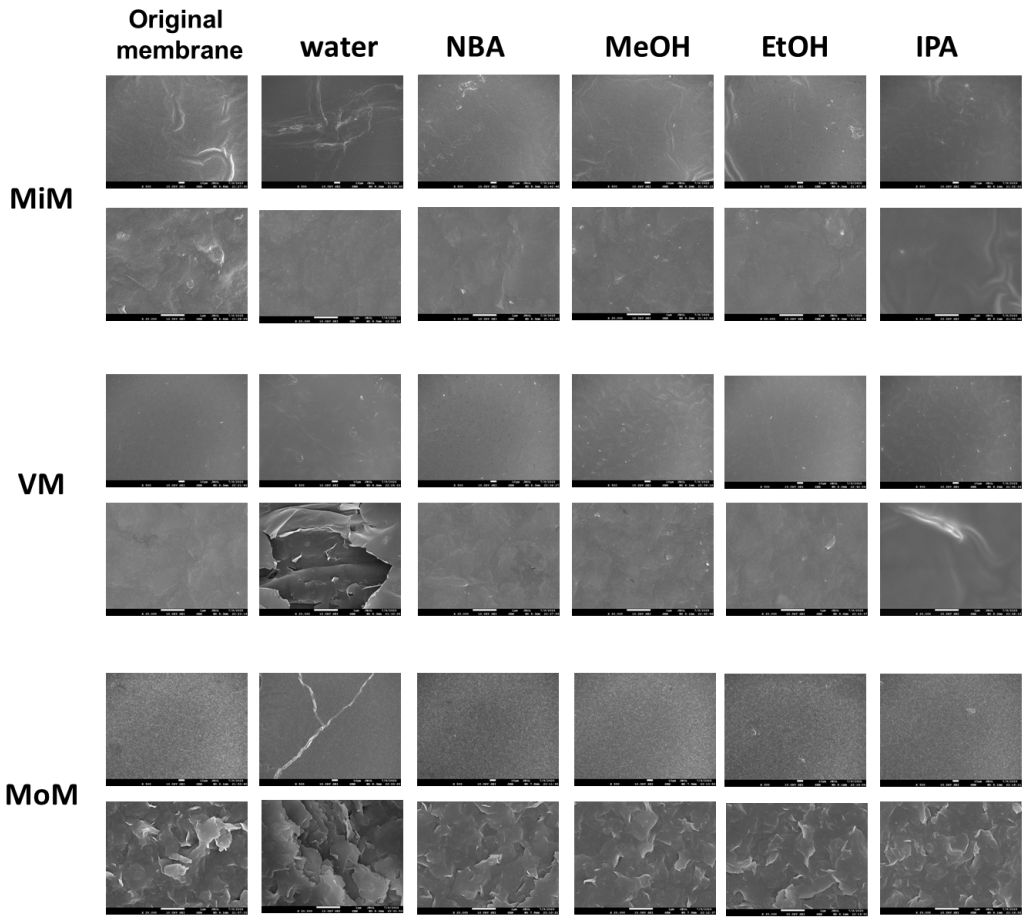

Figure S11. SEM images of the MiM, VM, and MoM after immersion in various solvents.

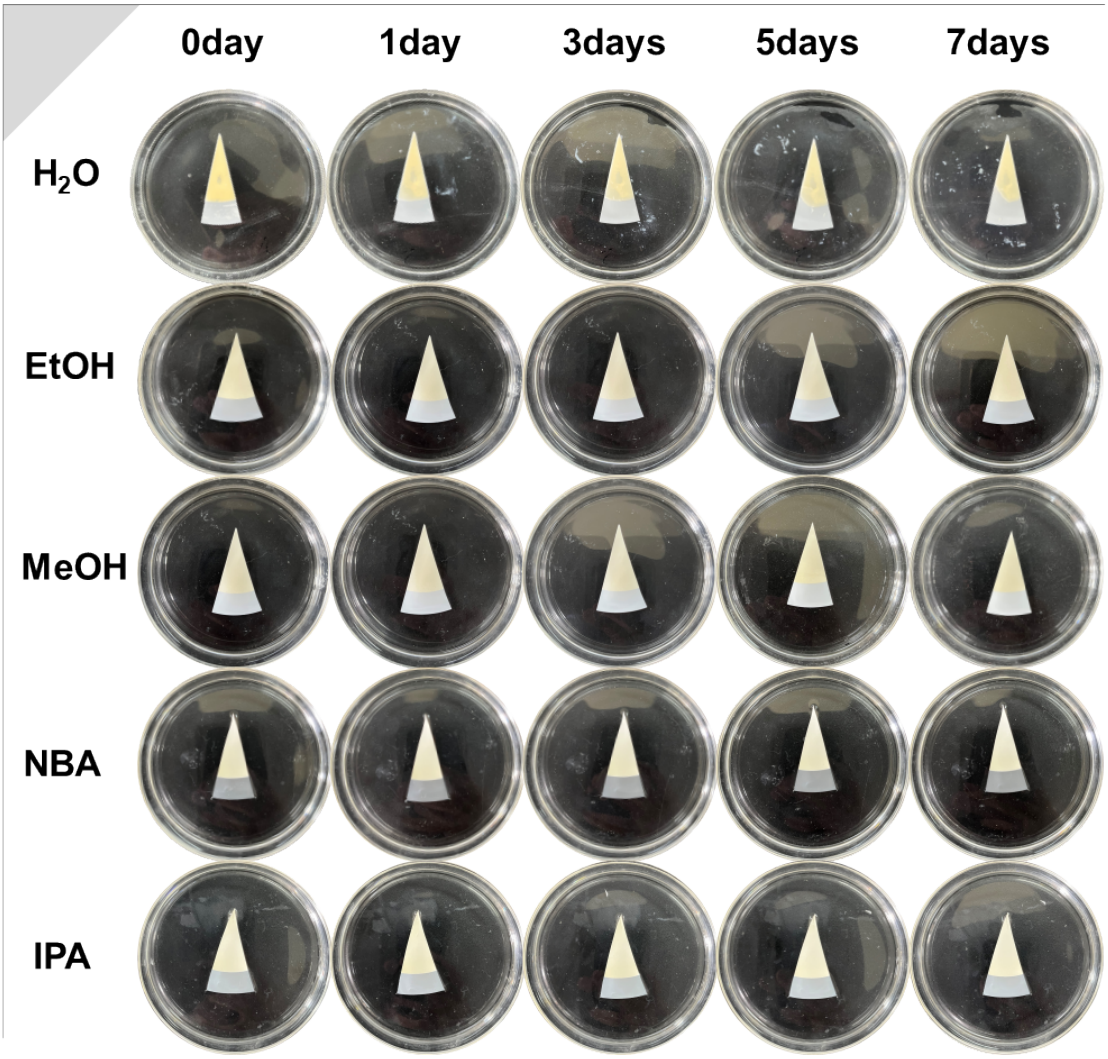

Figure S12. Photographs showing the changes in MiM, VM, and MoM after long-term immersion in various solvents.

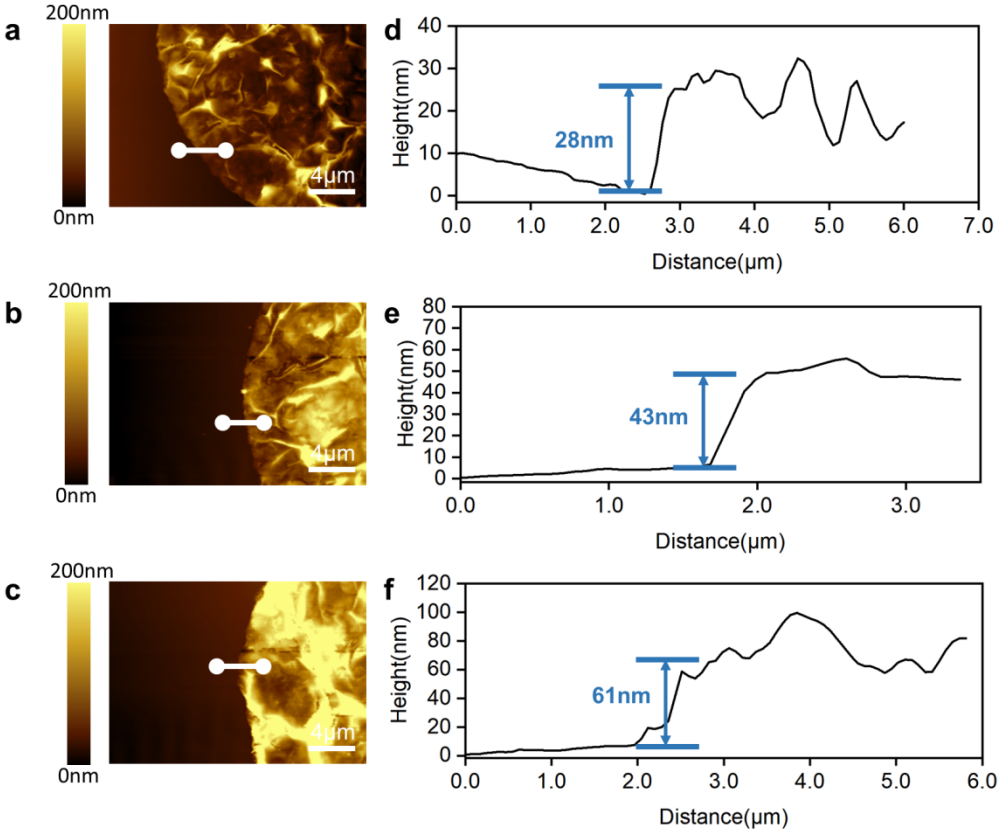

Figure S13. (a-c) AFM images of mica membranes with 0.1, 0.2, and 0.3 mg loading, (d-f) cross-sectional membrane thickness distribution of the white dashed lines.

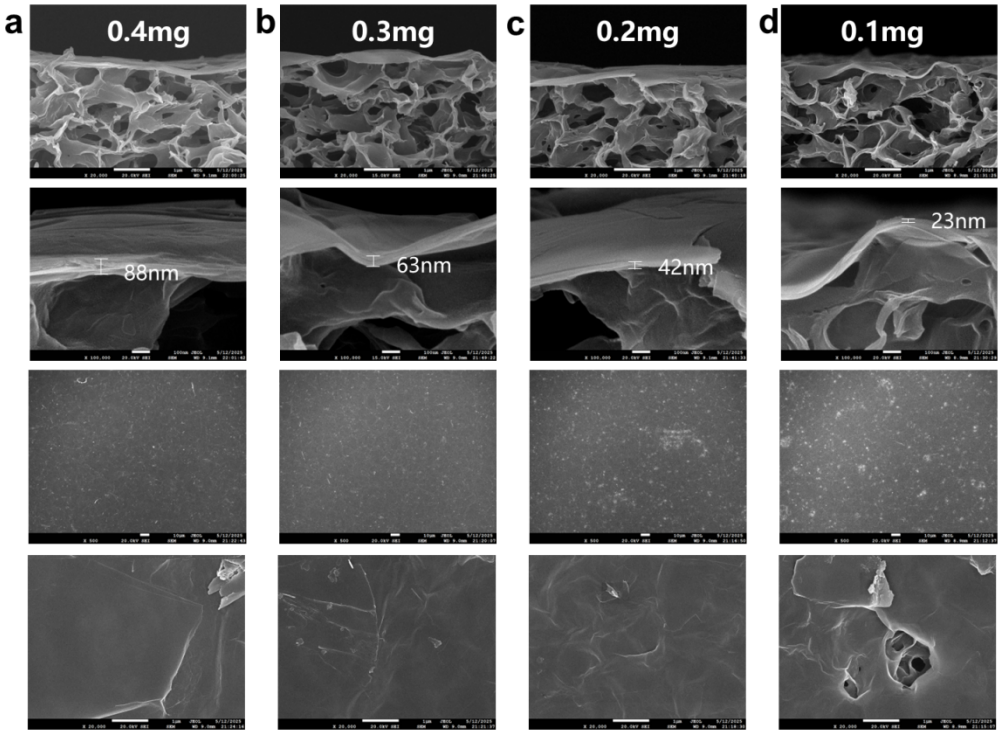

Figure S14. SEM cross-sectional and top-view images of MiM with 0.1, 0.2, 0.3, and 0.4 mg loading, showing the thickness of the membrane loading layers.

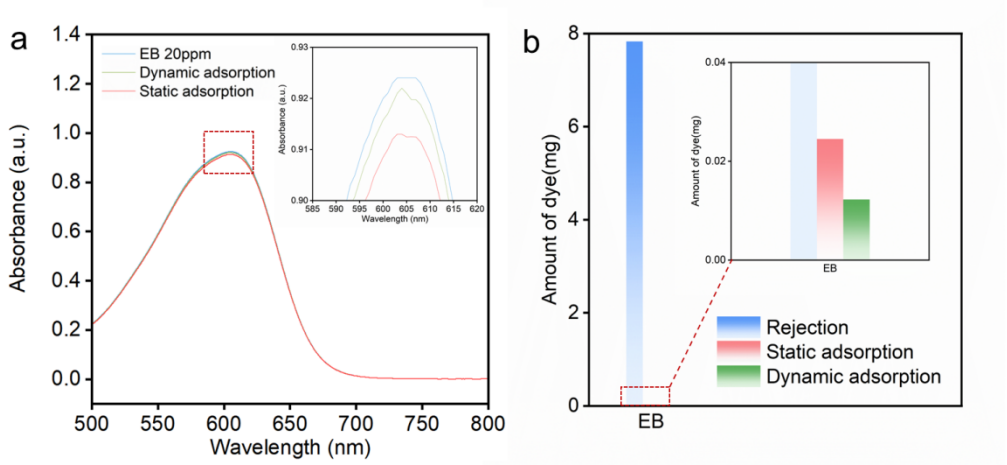

Figure S15. (a) UV/V absorption spectra of mica membrane after static and dynamic adsorption in Evans Blue methanol solution, with the inset showing a magnified view of the red boxed area; (b) Comparison of the dye mass adsorbed by the mica membrane under static and dynamic conditions in Evans Blue methanol solution with the mass of dye retained under the same time period, with the inset showing a magnified view of the red boxed area.

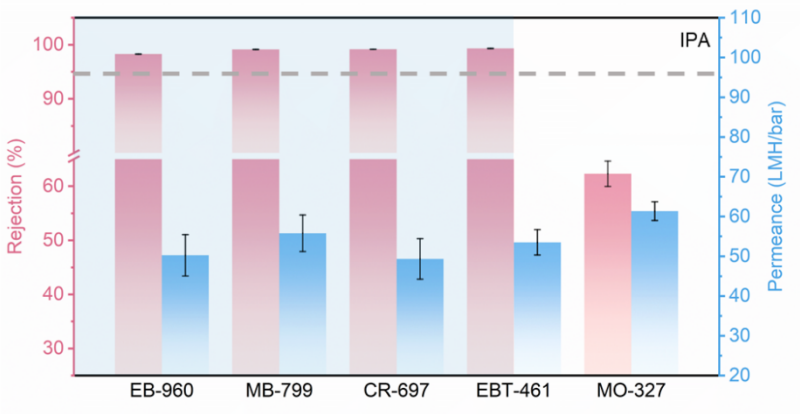

Figure S16. Comparison of dye rejection tests of MiM in isopropanol solutions.

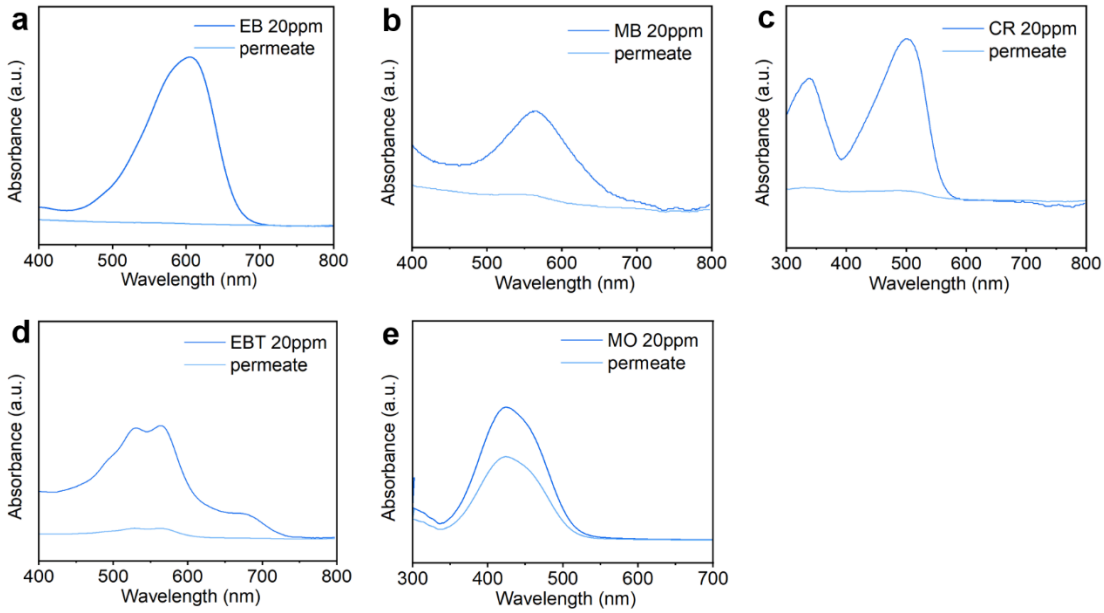

Figure S17. UV/V absorption spectra of EB, MB, CR, EBT, and MO of methanol solutions and permeate by using MiM.

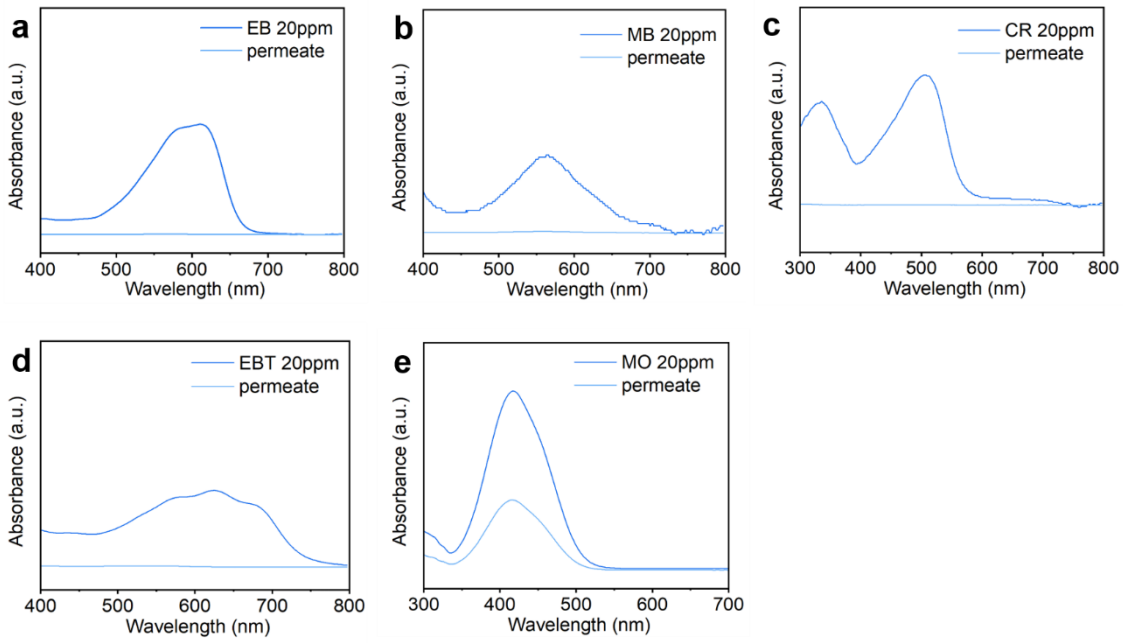

Figure S18. UV/V absorption spectra of EB, MB, CR, EBT, and MO of isopropanol solutions and permeate by using MiM.

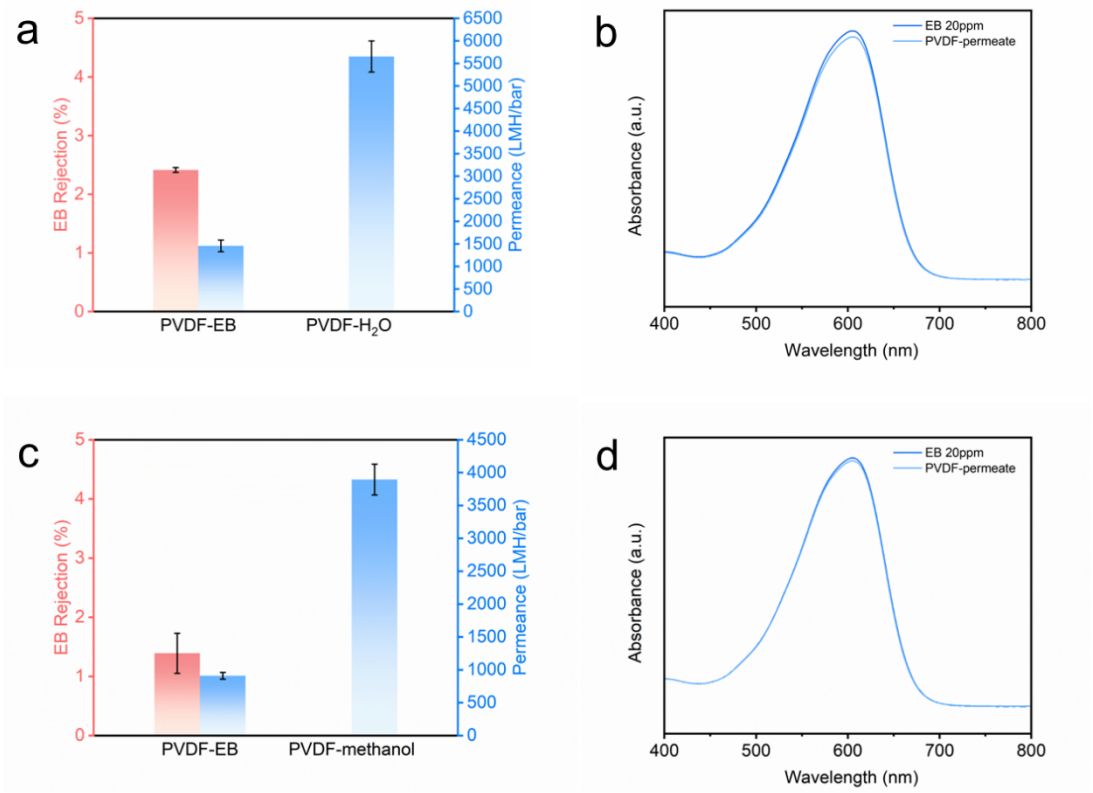

Figure S19 (a) Nanofiltration performance of the PVDF membrane for water and EB aqueous solution. The water flux was 5654.55 LMHB, while the EB aqueous solution flux was 1456.2 LMHB, with a retention rate of 2.415%, showing almost no retention effect, and no direct impact on the flux of the loaded layer; (b) Comparison of UV-visible absorption spectra of feed and permeate after testing the PVDF membrane. (c) Nanofiltration performance of the PVDF membrane for methanol and EB methanol solution. The pure water flux was 3893.7 LMHB, while the EB methanol solution flux was 908.8 LMHB, with a retention rate of 1.39%, showing almost no retention effect, and no direct impact on the flux of the loaded layer; (d) Comparison of UV-visible absorption spectra of feed and permeate after testing the PVDF membrane.

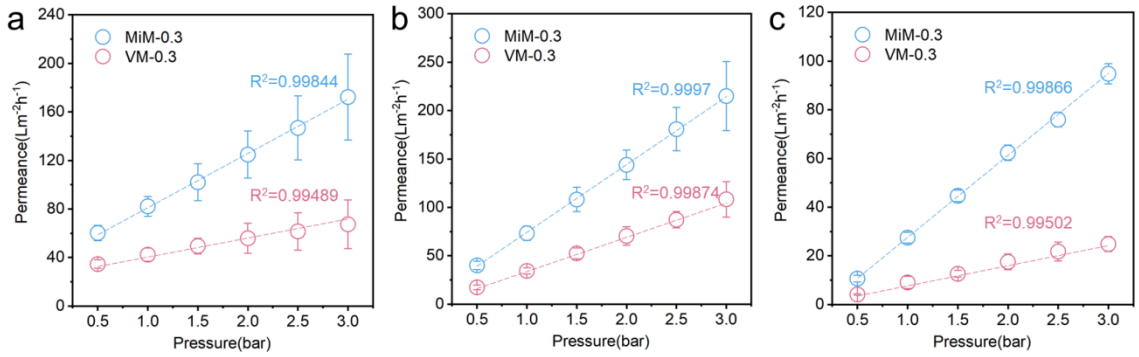

Figure S20. (a-c) Relationship between flux and pressure for mica and vermiculite membranes in pure water, methanol, and isopropanol, with the dashed lines representing the linear fitting results.

Table S1. Kinetic diameter and viscosity of the selected solvents solvents, and the permeance of MiM and VM in different solvents.

Solvent	Viscosity (mPa.s)	VM-Permeance (LMH/bar)	MiM-Permeance (LMH/bar)
acetonitrile	0.369	57.66	144.5
methanol	0.544	44.65	102.34
water	0.916	39	83.29
ethanol	1.074	28.13	50.93
isopropanol	2.038	16.1	47.5
1-Butanol	2.95	10.31	29.46

Table S2. Comparison of dye separation performance of MiM against state-of-the-art membranes in methanol under nanofiltration.

Membrane	Thickness	Solute	Solute MW (g/mol)	Concn. (ppm)	Methanol Permeance (LMHB)	Rejection (%)	Stability testing time (Methanol) (hours)	Stability testing time (Dye solution) (hours)	Ref.
HLGO	8 nm	CG	249	200	6.8	100	-	-	3
		DR	314		6.6	100			
		MLB	320		6.3	100			
		CV	408		6.5	100			
		BB	826		6.6	100			
		RB	1018		7	100			
GO-Mg^{2+}	200nm	CG	249		55	80			
		MLB	320		47	84			
		CV	408		47	88			
		RB	1018		41	94			
SFGO-La^{3+}	70nm	MO	327	10	~89	~44	-	72	4
		AF	586		97.39	95.03			
		AR	1018		106.82	95.73			
		AB	1299		97.4	>99.9			
LFGO-La^{3+}		AF	586		33.72	97.5			
		AR	1018		40.32	99.13			
		AB	1299		34.14	>99.9			
vermiculite Membrane (VMT)	15 nm	EB	961	20	30.1	99.7	-	13	5
GO/MXene	140 nm	MO	327	10	~20	~23	48	12	6
		MB	374		~18	~22			
		AY14	449		~18	~23			
rGO-$TMPyP_{0.6}$-44	36.2nm	EB	961	10	~13.03	93	24	-	7
		BY	624.5			84			
		AF	586			73.1			
rGO-44	33.9nm	EB	961		~1.62	99.9			
		BY				96.8			
		AF	586			94.5			
GO/PWs	260nm	CR	697	10	91.3	90.2	-	-	8
		BrB	624		~105	~88			
		RhB	479		~80	~85			
		BrG	698		~83	~80			
		MB	374		~75	~72			
GO_{DMSO}	393nm	EB	961	200	65.3	98.3	-	-	9
GO_{NMF}	373nm				50.8	99.3			

GO_{DMF}	324nm				27.1	99.7			
γ-MXT（Mxene membrane）	181.3nm	CR	697	10	100	41.2	-	-	[10]
		RhB	479		91.6	46.8			
		MB	374		95.6	45			
u-$Ti_3C_2T_x$@P84 $MMMs_{70}$	265nm	BBR	826		3.97	96.1	-	50	[11]
TK-TPC	36.8nm	SOG	214.2	100	12.97	15.11	120	-	[12]
		MO	327.3		12.65	97.50			
		RB	479		14.12	99.07			
		ACF	585.5		12.37	99.19			
		CR	696.6		13.80	96.60			
		AR	1017.6		14.01	99.23			
ODA/TMC	12nm	RB 19	626.5	50	36.9	56.6	16	-	[13]
MiM	43nm	EB	961	20	97.43	96.88	108	24	This Work
		MB	800		96.67	95.36			
		CR	696.6		94.78	88.54			

References

1. L. Y. Zhao, X. K. Wang, N. Z. Wu and Y. C. Xie, *Colloid and Polymer Science*, 2005, **283**, 699-702.
2. R. K. Joshi, P. Carbone, F. C. Wang, V. G. Kravets, Y. Su, I. V. Grigorieva, H. A. Wu, A. K. Geim and R. R. Nair, *Science*, 2014, **343**, 752-754.
3. Q. Yang, Y. Su, C. Chi, C. T. Cherian, K. Huang, V. G. Kravets, F. C. Wang, J. C. Zhang, A. Pratt, A. N. Grigorenko, F. Guinea, A. K. Geim and R. R. Nair, *Nature Materials*, 2017, **16**, 1198-1202.
4. L. Nie, K. Goh, Y. Wang, J. Lee, Y. Huang, H. E. Karahan, K. Zhou, M. D. Guiver and T.-H. Bae, *Science Advances*, 2020, **6**, eaaz9184.
5. M. Tian, L. Wang, J. Wang, S. Zheng, F. Wang, N. Shao and L. Wang, *ACS Sustainable Chemistry & Engineering*, 2022, **10**, 1137-1148.
6. S. Wei, Y. Xie, Y. Xing, L. Wang, H. Ye, X. Xiong, S. Wang and K. Han, *J Membrane Sci*, 2019, **582**, 414-422.
7. T. Gao, L. Huang, C. Li, G. Xu and G. Shi, *Carbon*, 2017, **124**, 263-270.
8. Z. He, G. Liu, M. Huang, C. Wang, J. Hu and Y. Li, *Colloids and Surfaces A: Physicochemical and Engineering Aspects*, 2022, **654**, 130066.
9. M. Zhang, P. Li, M. Li, W. Zheng, G. Xie, X. Xu, C. Liu and J. Jia, *J Membrane Sci*, 2021, **640**, 119841.
10. J. Li, Y. Li, H. Luo, L. Tang, N. Xu, W. Ji, S. Zhang, P. Nian and Y. Wei, *J Membrane Sci*, 2025, **722**, 123859.
11. Y. Shen, A. Yao, J. Li, D. Hua, K. B. Tan, G. Zhan and X. Rao, *J Membrane Sci*, 2023, **666**, 121168.
12. C. Liu, X. Feng, K. Zhang, X. Tian, Q. Wang, Y. Tang, Y. Yu, T. Gu, R. Zhang, X. Liu and S. Wang, *J Membrane Sci*, 2025, **726**, 124085.
13. H. Wu, Y. Xu, Q. Tang, B. Wu and P. Wu, *Nature Communications*, 2025, **16**, 8414.